Optics Letters

Multi-spectral infrared camouflage through excitation of plasmon-phonon polaritons in a visible-transparent hBN-ITO nanoantenna emitter

EBRU BUHARA,[1,2] AMIR GHOBADI,[1,2] AND EKMEL OZBAY[1,2,3,4,*]

[1]NANOTAM-Nanotechnology Research Center, Bilkent University, Ankara 06800, Turkey
[2]Department of Electrical and Electronics Engineering, Bilkent University, Ankara 06800, Turkey
[3]Department of Physics, Bilkent University, Ankara 06800, Turkey
[4]UNAM-Institute of Materials Science and Nanotechnology, Bilkent University, Ankara 06800, Turkey
*Corresponding author: ozbay@bilkent.edu.tr

Received 15 July 2021; revised 5 September 2021; accepted 6 September 2021; posted 13 September 2021 (Doc. ID 437933); published 30 September 2021

In an ideal platform for camouflage compatible cooling, the thermal emitter should be a spectrally selective antenna to radiate its heat buildup without being detected by thermal cameras. Moreover, to keep its visual appearance and to minimize solar induced heating, the structure should be visibly transparent. In this Letter, to achieve the visually invisible mid-infrared (MIR) camouflage-cooling feature, a metasurface design based on an indium-doped tin oxide (ITO)-hexagonal boron nitride (hBN) heterostructure is proposed. The proposed ITO-hBN nanoantenna shows spectrally selective broadband absorptions in near-infrared (NIR) and non-transmissive (MIR) windows, while it is dominantly non-emissive in other ranges. The camouflage ability of the structure in the targeted wavelengths is demonstrated using power calculations.

https://doi.org/10.1364/OL.437933

Based on the Stefan–Boltzmann law $P = \varepsilon\sigma T^4$, the emission from an object is a function of surface emissivity (ε). Based on Kirchhoff's law for thermal radiation, absorptivity of an object is equal to its emissivity, $\alpha(T, \lambda) = \varepsilon(T, \lambda)$. Thus, the manipulation of the absorption spectrum of a nanoantenna can be used as a means to design a proper thermal emitter design [1].

While obtaining thermal camouflage is possible by blocking all the emission wavelengths (for instance, using metallic foils), it causes heat buildup and instability issues. To prevent this, the emitted power should be selectively sent out into the atmosphere in some permitted wavelengths in the non-transmissive atmospheric windows [2,3]. There are two windows that allow transmission in the infrared region: 3–5 μm [mid-wave infrared (MWIR)] and 8–12 μm [long-wave infrared (LWIR)] ranges. Consequently, the non-transmissive infrared (NTIR) window locates at 5–8 μm wavelengths. Besides this, short-wave infrared (SWIR) (0.9–1.7 μm) cameras are also used for a target tracking. Unlike MWIR and LWIR mode designs, SWIR cameras detect the surface reflected solar irradiation rather than the blackbody emission. Thus, in an ideal camouflage compatible radiative cooling scenario, the object should be (i) SWIR absorber, (ii) MWIR and LWIR reflector, (iii) NTIR absorber, and (iv) visible transparent to keep its visual appearance and to minimize solar induced heating. The use of metal-based metamaterial/metasurface nanoantennas is a common approach to acquire suppressed emission in MWIR and LWIR regions while allowing radiative cooling in the NTIR window [4–7]. However, metallic designs do not meet the transparency and SWIR absorbing requirements. Excitation of surface plasmon polaritons (SPPs) in indium tin oxide (ITO) film using a nanounit design is an excellent choice [8,9]. Moreover, polar materials such as hexagonal boron nitride (hBN) can provide selective mid-infrared (MIR) absorption through excitation of hyperbolic phonon polaritons (HPPs), while maintaining high transparency in visible range (E_g of 6.1 eV, and n of ∼1.85 [10,11].

In this Letter, a hybrid nanoantenna architecture made of ITO-hBN grating is proposed to satisfy all multi-spectral camouflage requirements. In this design, simultaneous excitation of plasmon-phonon polaritons in ITO and hBN leads to broadband absorption in the NTIR range and reflection in MWIR and LWIR ranges. Moreover, the bulk absorption in ITO film provides SWIR mode camouflage. Moreover, to highlight the importance of this hybrid design, the ITO-hBN design is compared with ITO-TiO_2 heterostructure (TiO_2 is a lossless dielectric in our desired ranges). Finally, the camouflage performance of the metasurface is evaluated as the outgoing emission suppression when the metasurface design is on top of the blackbody object.

Figure 1(a) shows the schematic representation of an ITO-TiO_2 MIR absorber. The ITO is a 1-μm-thick layer, and the TiO_2 is a grating with width of w, height of t, and periodicity of P. To simulate the design, the commercial finite-difference time-domain (FDTD) software package (Lumerical FDTD Solutions) is utilized [12]. These simulations are carried out at two-dimensional (2D) environment, the incident light direction is in the y direction, the boundary conditions for the y and z directions are the periodic and perfectly matched layer (PML),

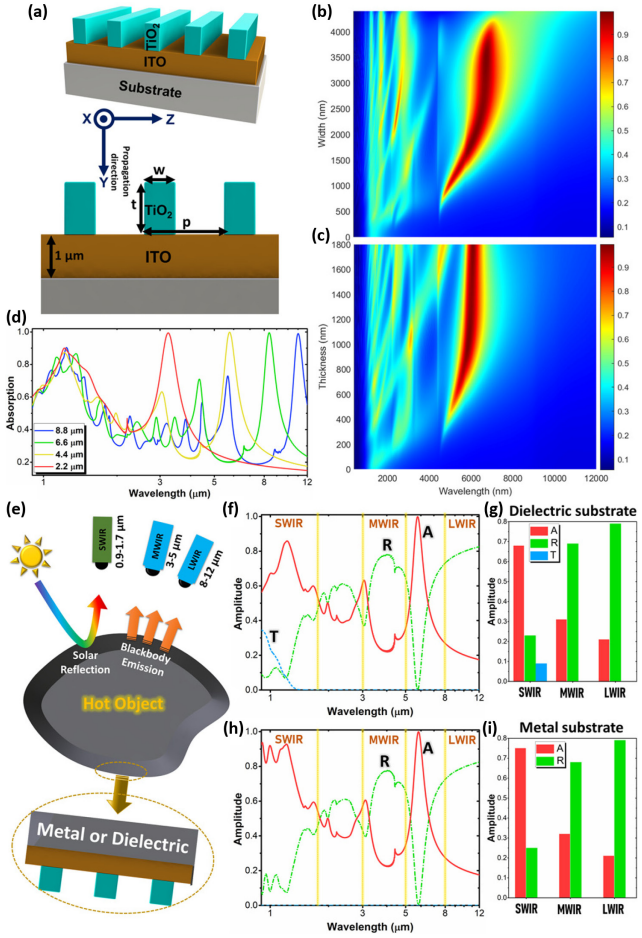

Fig. 1. (a) Schematic illustration of the nanoantenna design and the absorption contour plots for different (b) w and (c) t. (d) The dependence of the absorption profile to design periodicity. (e) Different detection scenarios of an object. The profiles and their average SWIR, MWIR, and LWIR absorption/reflection/transmission data of the nanoantenna on different substrates of (f)–(g) dielectric and (h)–(i) metal.

respectively. The permittivity of ITO is extracted from [13] and TiO_2 from [14]. First, the absorption contour plots versus width and the thickness of the grating are extracted, as shown in Figs. 1(b) and 1(c). In these simulations, the period of the design is chosen as $P = 4.4$ μm. The resonance wavelength (λ_{res}) (at normal incidence) in a metal-dielectric plasmonic design can be expressed as follows [15]:

$$\lambda_{res} = \mp \frac{P}{m} \sqrt{\frac{\varepsilon_{metal} . n_{eff}^2}{\varepsilon_{metal} + n_{eff}^2}}, \quad (1)$$

where P is periodicity, m is the diffraction order, and n_{eff} is the effective refractive index of the SPP mode. In the other side, the n_{eff} is directly proportional to grating filling factor (or grating width) [16]. This can be seen in Fig. 1(b). Moreover, it is shown that, upon grating height increase, the n_{eff} is gradually increased up to some point, and from there it experiences a saturation. This is due to the fact that SPP fields exponentially decay within the grating; after some thickness, they do not see any change in the surrounding environment, and consequently the mode index saturates [17]. This is exactly what we see in Fig. 1(c). Thus, in our case, the alternative plasmonic material, which is ITO, triggers the excitation of SPP modes in the MIR region. To have a strong emission in the NTIR window with minimal signature in MWIR and LWIR ranges, the optimal geometries are chosen as $w = 1600$ nm and $t = 900$ nm. Moreover, it should be mentioned that the proposed design is a universal solution to achieve MIR resonant absorption with high optical transparency. To show this, the absorption of the design is simulated for different P values while the w/P and w/P ratios are kept same. As we can see from Fig. 1(d), the near perfect absorption resonance in the MIR region is linearly shifted toward longer wavelengths as we increase the periodicity.

The detection mechanisms based on thermal imaging are schematically shown in Fig. 1(e). Our above findings prove the functionality of the proposed nanoantenna in spectrally selective engineering of the emitted power. However, it is essential to evaluate its performance on different types of hosts. For this aim, we used two extreme substrate cases of metal and dielectric. The absorption (A), reflection (R), and transmission (T) data for both cases are depicted in Figs. 1(f) and 1(h). Overall, both designs are dominantly reflective in MWIR and LWIR ranges and have spectral absorption/emission in NTIR range. However, their responses in SWIR range slightly differ. Unlike MIR range, ITO is a low-loss low-index medium in the SWIR regime. Thus, the absorption mechanism is simply the bulk absorption within the ITO film. Therefore, due to the metallic mirror, the optical path length of light within the ITO is enhanced, and consequently larger average absorption values are achieved. The average A, R, and T data have been extracted for both cases in SWIR, MWIR, and LWIR ranges. As seen from Figs. 1(g) and 1(i), in LWIR and MWIR frequency span, near 80% and 70% of light is reflected, proving its suppressed signature in these ranges. In SWIR, the dielectric platform imposes ~67% absorption while metallic substrate absorbs near 76% of the incoming light. It should be noted that the A/R/T profiles of a bare ITO are also shown in Fig. S1 in Supplement 1, where the SWIR response is the same as the nanoantenna but no emission (radiative cooling) in NTIR range is seen.

In the next step, we replaced the dielectric grating with a polar material, hBN. Originating from its optical phonon vibrations, hBN naturally possesses MIR Reststrahlen (RS) bands, and one of these bands is located in the NTIR regime. Because of the hyperbolicity in these RS bands, hBN films support multiple orders of low-loss HPP waveguide modes that can potentially be employed to acquire spectrally selective MIR absorption. Thus, the right use of hBN grating on ITO film can provide broader emission (compared to TiO_2 case) in NTIR region without disturbing its camouflage performance and visible transparency. This architecture can simultaneously excite SPPs in ITO-hBN and HPPs in hBN-air interfaces. The proposed design is exhibited in Fig. 2(a). Moreover, the hBN permittivity (both in plane and out of plane parts) is compared with TiO_2. As Fig. 2(b) implies, the hBN has its RS band in NTIR region, and in the rest of spectrum, it is a lossless dielectric with a permittivity close to TiO_2. The R and A responses of optimized TiO_2-based and hBN-based thermal nanoantenna emitters have been compared in Fig. 2(c). The optimal dimensions of P, w, and t for hBN were found as 5.5 μm, 1.2 μm, and 1.3 μm. The hBN design has a multiple resonant absorption response in the NTIR region ($\lambda_1 = 6.15$ μm, $\lambda_2 = 6.82$ μm, $\lambda_3 = 7.2$ μm), while it keeps its reflective behavior in the MWIR and LWIR

ranges. Moreover, the visible light response of ITO-hBN shows the visual transparency of the design [see Fig. 2(d)]. To understand the origin of these resonant modes, parametric sweep on grating width, height, and periodicity is used, as depicted in Figs. 2(e)–2(g). These contour plots imply that the origin of these resonance modes is different. To gain an insight, the electric field and absorption profiles across the design are extracted for both SWIR and NTIR resonances. As Fig. 2(h) plots, the excitation of Fabry–Perot modes is the dominant absorption mechanism, which leads to the bulk absorption within the ITO layer. At the λ_1 resonance, a dipolar field profile with two hot spots in the grating edge is observed, and the absorption is dominantly concentrated in the hBN grating [see Fig. 2(i)]. The decaying absorption profile (from the air into the hBN bulk), besides hBN optical properties, shows that this mode is a HPP. Due to this nature, the grating width imposes a slight redshift (corresponding to the decay length of HPPs in the air-hBN interface) [Fig. 2(e)], and periodicity does not affect its spectral position [Fig. 2(g)]. The vector field profile of the second mode, λ_2, shows simultaneous excitation of the HPP mode in the hBN wall, and the SPP mode in the hBN-ITO interface. This is also reflected in their absorption profile, where both ITO and hBN are active absorbers [Fig. 2(j)]. Thus, this mode is a hybrid SPP-HPP mode, and the gradual redshift, seen in Fig. 2(e), is due to change in n_{eff} of the grating as explained in Eq. (1). Finally, at 7.2 μm, the hBN layer has small Im(ε), and it acts like a high-index lossless dielectric and excites the SPPs in the ITO layer, as seen in Fig. 2(k).

To demonstrate the camouflage character of the design, the metasurface is placed on top of a blackbody radiator (BB) with emissivity of unity [see Fig. 3(a)]. The thermal emission from the dotted box is modeled as the sum of three different emissions shown in Eq. (2). The first one is the design's own emission calculated using Eq. (3). The second one is the transmitted from

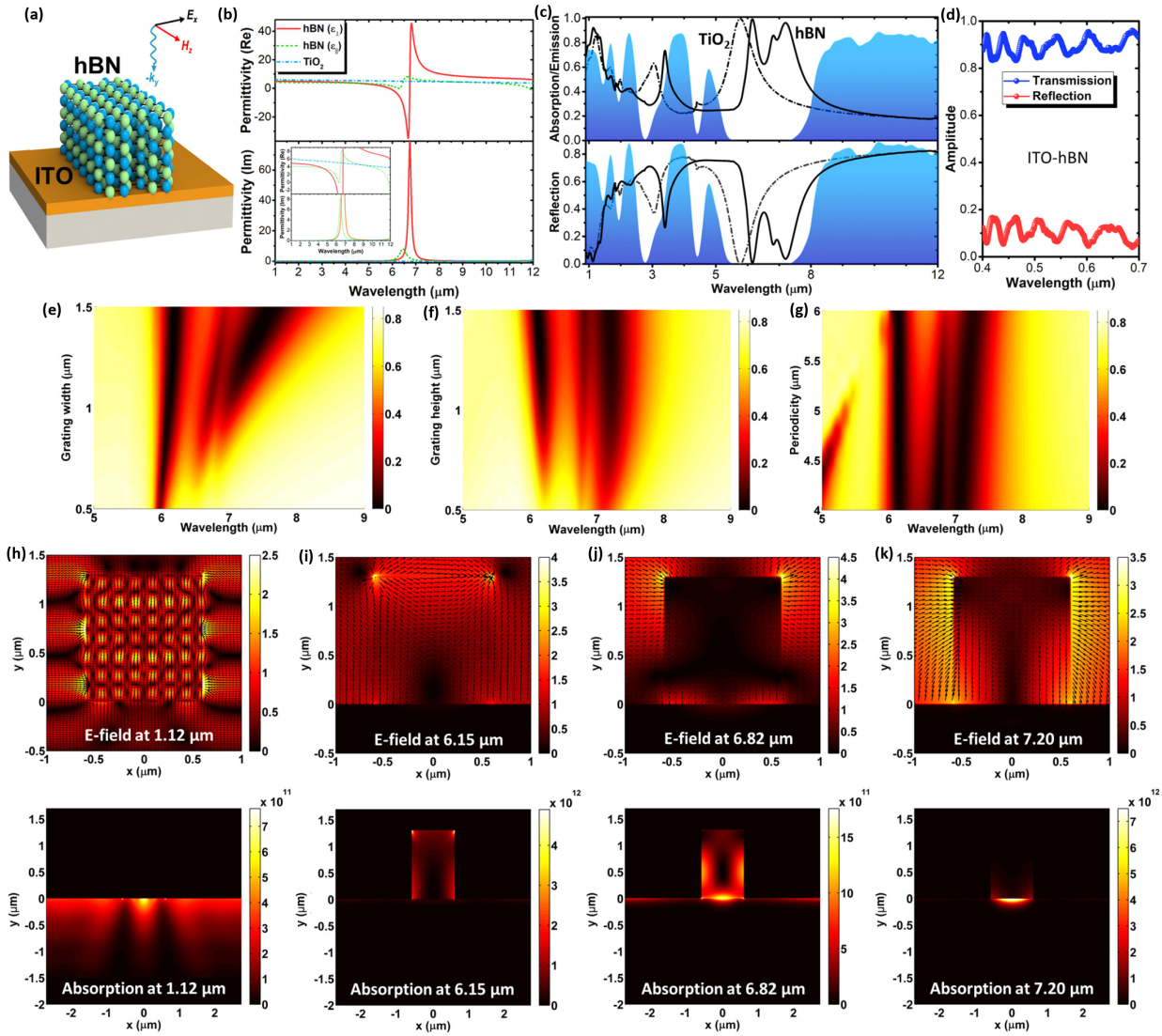

Fig. 2. (a) Proposed hBN-ITO nanoantenna design, (b) permittivity data of hBN and TiO_2, and (c) absorption/reflection spectra of the nanoantenna for both hBN- and TiO_2-based designs. (d) Visible light transmission and reflection of ITO-hBN. The reflection contour plots of the nanoantenna design as a function of grating (e) width, (f) height, and (g) periodicity. The E-field and absorption density profiles across the nanoantenna for different resonance wavelengths of (h) 1.12 μm, (i) 6.15 μm, (j) 6.82 μm, and (k) 7.2 μm. The color bar units for E-field and absorption density are V/m and W/m^2.

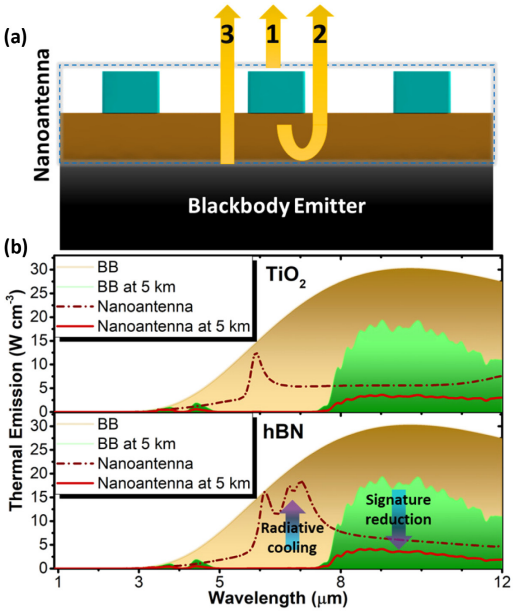

Fig. 3. (a) Schematic illustration of thermal emission pathways from the design on top of a blackbody. (b) Thermal emission comparison of blackbody radiation at room temperature, blackbody radiation under the atmospheric transmission, metasurface design on top of BB, and the real emission from the design.

the design, reflected from the BB and back-transmitted through the metasurface, which is demonstrated in Eq. (4). The final one is the emission from the BB transmitted through the design in Eq. (5). The blackbody radiation is calculated as in Eq. (6). The thermal emission of the design is the multiplication of Eqs. (2) and (6), which is shown in Eq. (7),

$$\varepsilon_{\text{eff}}(T,\lambda) = \sum_{j=1}^{3} \varepsilon_j(T,\lambda), \tag{2}$$

$$\varepsilon_1(T,\lambda) = 1 - R(T,\lambda) - T(T,\lambda), \tag{3}$$

$$\varepsilon_2(T,\lambda) = \left(1 - \varepsilon_{\text{blackbody}}\right) T_{\text{back}}(T,\lambda)\,\varepsilon_1(T,\lambda), \tag{4}$$

$$\varepsilon_3(T,\lambda) = T_{\text{back}}(T,\lambda)\,\varepsilon_{\text{blackbody}}, \tag{5}$$

$$BB(T,\lambda) = \frac{2\pi hc^2}{\lambda^5\left(e^{\frac{hc}{\lambda kT}} - 1\right)}, \tag{6}$$

$$TE(T,\lambda) = \varepsilon_{\text{eff}}(T,\lambda) \times BB(T,\lambda). \tag{7}$$

Due to the optically thick ITO, no light transmission is occurred; thus, T_{back} is zero. The radiated power, in a distance of R, is calculated as $TE(R, T, \lambda) = T_{\text{atm}}(R,\lambda) \times TE(T,\lambda)$, where $T_{\text{atm}}(R,\lambda)$ is the atmospheric transmission at this distance [18]. Using these equations, the spectral emission of BB (300 K) at the surface, BB at 5 km, nanoantenna covered BB at the surface, and nanoantenna covered BB at 5 km have been calculated and compared for both TiO_2 and hBN in Fig. 3(b). Radiated powers of the BB, TiO_2, and hBN are shown in Table 1. The TiO_2-based and hBN-based nanoantenna has reduced BB emission by 71% and 64% in the MWIR range. This reduction is about 81% in the LWIR range. Moreover, the emission at the surface in the NTIR range shows that hBN has not only better camouflage performance but also stronger cooling character [see Fig. 3(b)].

Table 1. Radiated Amount of Emission

Power Density ($J/m^2 \cdot s$)	BB	TiO_2	hBN
3–5 μm (at 5 km)	1.3214	0.4785	0.4030
5–8 μm (at surface)	55.9562	16.7719	29.9525
8–12 μm (at 5 km)	61.8909	12.2986	12.2847

In conclusion, this study demonstrates a visible-transparent infrared selective emitter capable of multi-spectral camouflage in SWIR, MWIR, and LWIR modes. The proposed design can also radiatively cool itself in the NTIR windows.

Disclosures. The authors declare no conflicts of interest.

Data Availability. Data underlying the results presented in this Letter are not publicly available at this time but may be obtained from the authors upon reasonable request.

Supplemental document. See Supplement 1 for supporting content.

REFERENCES

1. H. Zhu, Q. Li, C. Tao, Y. Hong, Z. Xu, W. Shen, S. Kaur, P. Ghosh, and M. Qiu, Nat. Commun. **12**, 1805 (2021).
2. X. Feng, X. Xie, M. Pu, X. Ma, Y. Guo, X. Li, and X. Luo, Opt. Express **28**, 9445 (2020).
3. Y. Qu, Q. Li, L. Cai, M. Pan, P. Ghosh, K. Du, and M. Qiu, Light Sci. Appl. **7**, 26 (2018).
4. E. Buhara, A. Ghobadi, B. Khalichi, H. Kocer, and E. Ozbay, J. Phys. D **54**, 265105 (2021).
5. A. Kalantari Osgouei, H. Hajian, B. Khalichi, A. E. Serebryannikov, A. Ghobadi, and E. Ozbay, Plasmonics **16**, 1013 (2021).
6. B. Khalichi, A. Ghobadi, A. K. Osgouei, and E. Ozbay, J. Phys. D **54**, 365102 (2021).
7. A. K. Osgouei, A. Ghobadi, B. Khalichi, and E. Ozbay, J. Opt. **23**, 085001 (2021).
8. G. Dayal and S. A. Ramakrishna, Opt. Express **22**, 15104 (2014).
9. Y. Wang, A. C. Overvig, S. Shrestha, R. Zhang, R. Wang, N. Yu, and L. D. Negro, Opt. Mater. Express **7**, 2727 (2017).
10. B. Zhao and Z. M. Zhang, Opt. Express **25**, 7791 (2017).
11. B. Zhao and Z. M. Zhang, Int. J. Heat Mass Transfer **106**, 1025 (2017).
12. Lumerical Solution Inc., https://www.lumerical.com/.
13. D. U. Yildirim, A. Ghobadi, M. C. Soydan, O. Atesal, A. Toprak, M. D. Caliskan, and E. Ozbay, ACS Photon. **6**, 1812 (2019).
14. J. Kischkat, S. Peters, B. Gruska, M. Semtsiv, M. Chashnikova, M. Klinkmüller, O. Fedosenko, S. MacHulik, A. Aleksandrova, G. Monastyrskyi, Y. Flores, and W. T. Masselink, Appl. Opt. **51**, 6789 (2012).
15. M. Abutoama and I. Abdulhalim, IEEE J. Sel. Top. Quantum Electron. **23**, 72 (2017).
16. D. V. Nesterenko, S. Hayashi, and Z. Sekkat, Appl. Opt. **54**, 4889 (2015).
17. S. Randhawa, M. U. González, J. Renger, S. Enoch, and R. Quidant, Opt. Express **18**, 14496 (2010).
18. A. Berk, P. Conforti, R. Kennett, T. Perkins, F. Hawes, and J. van den Bosch, in *6th Workshop on Hyperspectral Image and Signal Processing: Evolution in Remote Sensing (WHISPERS)* (IEEE, 2014), pp. 1–4.